Preprint Title	Influence of Carrier Gas Flow Rate on the Synthesis of Long MWCNTs from Biorenewable Carbon Feedstock: α-Pinene.
Authors	Alexis Pérez Gasquez y Marín, Julián López-Tinoco, Javier Lara-Romero, Ricardo Rangel-Segura, Rafael Huirache-Acuña and Dario Stacchiola
Publication Date	16 März 2026
Article Type	Full Research Paper
ORCID® iDs	Julián López-Tinoco - https://orcid.org/0000-0002-7518-1737; Javier Lara-Romero - https://orcid.org/0000-0003-0216-364X; Rafael Huirache-Acuña - https://orcid.org/0000-0002-1395-0887

Influence of Carrier Gas Flow Rate on the Synthesis of Long MWCNTs from Biorenewable Carbon Feedstock: α-Pinene.

Alexis Pérez Gasquez y Marín[‡1], Julián López-Tinoco[‡1], Javier Lara-Romero[*1], Ricardo Rangel-Segura[‡1], Rafael Huirache-Acuña[‡1], Dario J. Stacchiola[‡2]

[1]Facultad de Ingeniería Química, Universidad Michoacana de San Nicolás de Hidalgo, Edificio V1, Ciudad Universitaria, 58060, Morelia, Michoacán, México and [2]Center for Functional Nanomaterials, Brookhaven National Laboratory, Upton New York, 11973-5000, USA

E-mail: Javier Lara-Romero - lararom@umich.mx

* Corresponding author

‡ Equal contributors

Abstract

This study investigates the efficient synthesis of millimeter-long multi-walled carbon nanotubes (MWCNTs) via the spray pyrolysis of a sustainable α-pinene/ferrocene precursor. The impact of carrier gas flow rate (2500, 5000, and 7500 sccm) on the morphology, purity, and structural integrity of the resulting nanotubes was systematically evaluated across different zones of a horizontal quartz reactor. Results indicate a clear trade-off between growth kinetics and crystalline quality. The maximum nanotube length of 1.416 mm was achieved at the lowest flow rate

of 2500 sccm, with length decreasing to 0.584 mm as the flow rate tripled. Conversely, comprehensive characterization using Raman spectroscopy, X-ray diffraction (XRD), and Thermogravimetric Analysis (TGA) revealed that the 5000 sccm flow rate produced the most thermally stable and highly crystalline structures. Spatial analysis across the furnace showed high uniformity in the central isothermal zones, while the entrance and exit sections exhibited higher residual metal content (up to 27.5 wt.%) and reduced crystallinity due to thermal gradients. These findings demonstrate that while lower flow rates favor longitudinal growth, moderate flow rates optimize the graphitic perfection of MWCNTs, providing a tunable pathway for the large-scale production of high-quality nanotubes from bio-derived precursors.

Keywords

Carbon nanotubes, α-pinene, length profile, spray pyrolysis, crystallinity

1. Introduction

Carbon nanotubes (CNTs) possess exceptional optical, electrical, thermal, and mechanical properties, making them pivotal for diverse scientific and industrial applications [1-3]. Research has extensively explored their integration into fields such as biology [4], biomedicine [5], electrical conductivity [6], superconductivity [7], hydrogen storage [8] and field emission displays [9]. However, the efficacy of these applications largely depends on the precise control of structural and morphological features, particularly crystallinity and length [10]. Synthesizing millimeter-long CNTs remains a significant challenge for their successful incorporation into macroscopic systems. Recent advancements have utilized various techniques to achieve high

aspect-ratio growth. For instance, high-precision pulsed laser deposition was used to prepare Fe/Mo catalytic films to produced CNTs of ~1.5 mm using ethylene as carbon source in a chemical vapor deposition reactor (CVD) [11]. A water-assisted chemical CVD using ethylene as carbon precursor and Fe, Al/Fe, Al_2O_3/Fe and Al_2O_3/Co films as catalytic substrates has produced nanotubes reaching 2.5 mm [12]. The CVD of ethylene on MgO crystals in the (110) plane orientation allowed the growth of 2.2 mm long CNTs [13]. The pyrolytic decomposition of benzene/ferrocene mixtures in a CVD system yielded 2.8 mm long CNTs [14]. Centimeter long CNTs (2.17 cm) were produced by water-assisted CVD of ethylene on Fe-Gd catalyst deposited on Al_2O_3/SiO_2/Si substrates [15]. While petroleum-derived compounds have historically served as the primary carbon source for these nanostructures, there is a growing shift toward renewable, botanical-derived precursors. Recent studies have successfully employed natural precursors such as camphor and camphor derivatives [16], eucalyptus oil [17], neem oil [18] and turpentine oil [19] as sustainable alternatives. Among these, α-pinene ($C_{10}H_{16}$), a bicyclic terpenoid hydrocarbon and the most abundant terpene in nature, presents a promising candidate. Primarily sourced from the distillation of turpentine, α-pinene is traditionally used in the synthesis of fragrances and pharmaceuticals. However, its high carbon content makes it an effective precursor for nanomaterials.

Building upon our previous reports on the synthesis of multi-walled carbon nanotubes (MWCNTs) via spray pyrolysis of turpentine and α-pinene, this study seeks to further optimize this green synthesis route. Specifically, we aim to establish the optimal carrier gas flow conditions required to achieve millimeter-long MWCNTs and to characterize the resulting length and crystallinity profiles along the reactor

axis of MWCNTs produced by the spray pyrolysis of α-pinene/ferrocene mixtures within the reaction system.

2. Experimental

The spray pyrolysis system used for the production of MWCNTs has been reported previously [20]. Briefly, it consists of a cylindrical furnace (Thermolyne 1200) equipped with a high precision temperature controller. A quartz tube connected to a commercial nebulizer is placed inside the furnace. α-Pinene and ferrocene (Sigma-Aldrich) were used as carbon source and catalyst respectively. From previous work, the synthesis temperature and ferrocene concentration to obtain a high yield of crystalline MWCNTs were fixed at 800° C and 37 mg/mL, respectively [21]. This mixture was fed into the quartz tube using high purity argon as carrier gas. Three carrier gas fluxes were evaluated: 2500, 5000 and 7500 standard cubic centimetres per minute (sccm).

Scanning electron microscopy (SEM) was used to accurately determine the length of the MWCNTs formed vertically aligned on the quartz tube. SEM images were obtained using a Jeol JSM-6400 scanning electron microscope. High-resolution transmission electron microscopy (HR-TEM) images of MWCNTs were obtained in a Jeol JEM-2200FS analytical microscope operating at 200 kV. Thermogravimetric analyses (TGA) were carried out in a Perkin Elmer Pyris 1. Samples were analyzed at a heating rate of 1ºC /min to 800ºC in an oxygen atmosphere flowing at 75 ml/min. Sample masses ranged from 5-10 mg and no special preparation was required. X-ray diffraction (XRD) analyses were carried out using a Panalytical X'Pert PRO

Diffractometer equipped with a curved graphite diffracted beam monochromator using a Cu Kα radiation (λ=1.54184 Å) at 43 kV and 30 mA. Finally, the Raman spectra were obtained with an iHR 320 Horiba Jobin Yvon spectrometer emitting at 532 nm with an output power of 25mW. The system is equipped with an Olympus BX41 optical microscope and a thermoelectrically cooled charge coupled detector (Synapse CCD Detection System) with 1024 × 256-pixel format operating at -70° C.

3. Results and Discussion

3.1 Morphological Characterization and Length Determination via SEM

The precursor materials and experimental setup are summarized in Figure 1. The molecular structures of the carbon source (α-pinene) and the organometallic catalyst (ferrocene) are shown in Figure 1a, while the spray pyrolysis configuration is illustrated in Figure 1b. To establish a precise longitudinal length profile, the quartz reaction tubes were partitioned into six 0.5 cm segments at specific distances from the inlet (0, 8, 16, 24, 32, and 40 cm), as depicted in Figure 1c.

Multiple vertical measurements were taken across the cross-sectional SEM micrographs for each reactor section to account for local height fluctuations in the MWCNT films. The uncertainty is expressed as the standard deviation (σ) calculated using the formula: $\sigma = \sqrt{\Sigma(x_i - \bar{x})^2/(n-1)}$, where x_i represents the individual section lengths and $\bar{x}$ is the mean length. A baseline systematic uncertainty (typically 1-2 %) was considered based on the SEM's calibration scale bar at the used magnification, though the statistical variance between sections remains the

dominant source of uncertainty. In all flows, the average excludes section 1 (the entrance zone) to accurately represent the steady-state growth region, as the initial section is influenced by the induction time of the reaction. The corresponding lengths of MWCNTs in each section at the three flows tested are summarized in Table 1.

Figure 2 presents cross-sectional SEM micrographs of the multi-walled carbon nanotubes (MWCNTs) synthesized at a flow rate of 2500 sccm. At this flow rate, the MWCNTs exhibit a relatively uniform length distribution across the reactor, with the exception of the first section. This initial reduction in growth can be attributed to the boundary layer effects and the induction time required for the thermal decomposition of α-pinene. At the furnace entrance, the lower local concentration of dissociated carbonaceous radicals limits the feedstock availability. As the precursors traverse the hot zone, the concentration of reactive species increases, leading to a steady-state growth rate and consistent tube lengths.

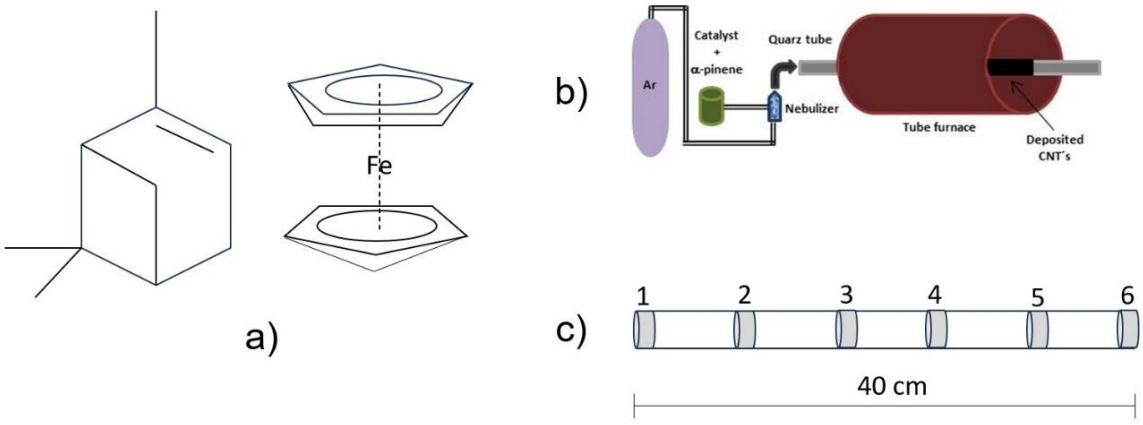

Figure 1: a) Chemical structures of α-pinene (carbon precursor) and ferrocene (catalyst); b) Schematic representation of the spray pyrolysis system; c) Layout of the six quartz tube segments analyzed for longitudinal growth profiles.

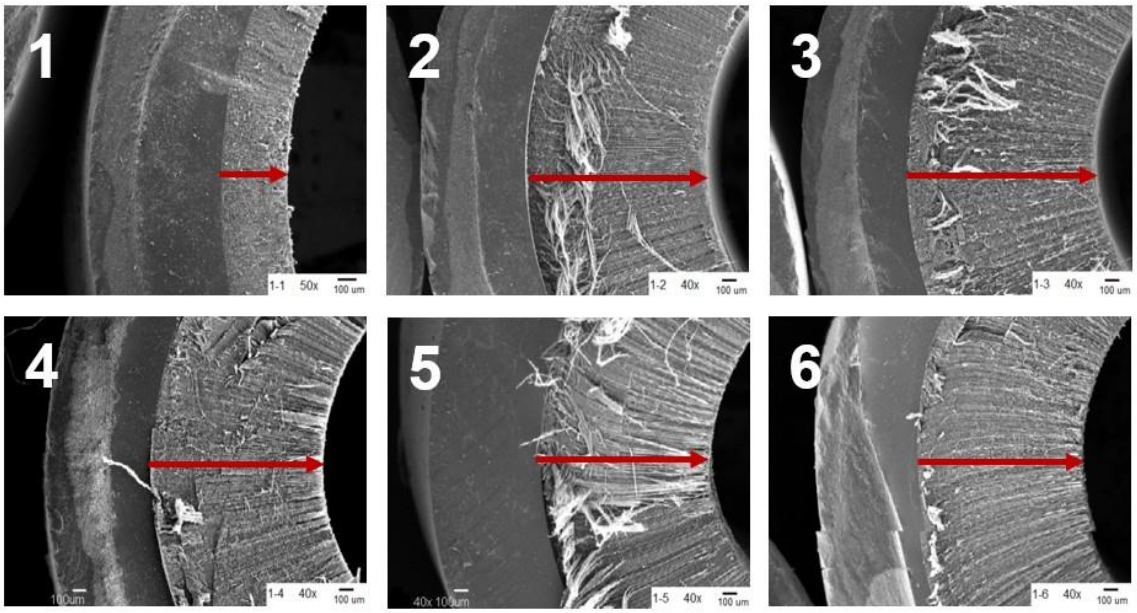

Figure 2: Cross-sectional SEM micrographs of MWCNT films synthesized at 800 °C with a carrier gas flow of 2500 sccm. Segment numbers correspond to the positions defined in Figure 1c. The red arrows indicate the MWCNT thickness and growth direction.

Table 1. Refined MWCNT film length with uncertainty estimates

Flow rate (sccm)	1	2	3	4	5	6	Average ± Uncertainty
2500	0.404	1.377	1.416	1.322	1.300	1.255	1.334 ± 0.028
5000	0.095	0.678	0.708	0.652	0.638	0.092	0.669 ± 0.015
7500	0.086	0.091	0.536	0.584	0.445	0.109	0.522 ± 0.041

3.2 Influence of Carrier Gas Flow Rate on Growth Kinetics

The effect of increasing the carrier gas flow rate to 5000 sccm is shown in Figure 3. MWCNT film lengths obtained in each section are reported in table 1. A significant decrease in MWCNT length is observed compared to the 2500 sccm samples. This inverse relationship between flow rate and length suggests that at higher velocities, the residence time of the carbon precursors within the reaction zone is reduced. Consequently, there is less time for the carbon fragments to interact with the catalyst particles, resulting in shorter structures. Similar to the previous case, the "edge effect" is present, where the MWCNTs at the extremities are shorter than those in the central sections.

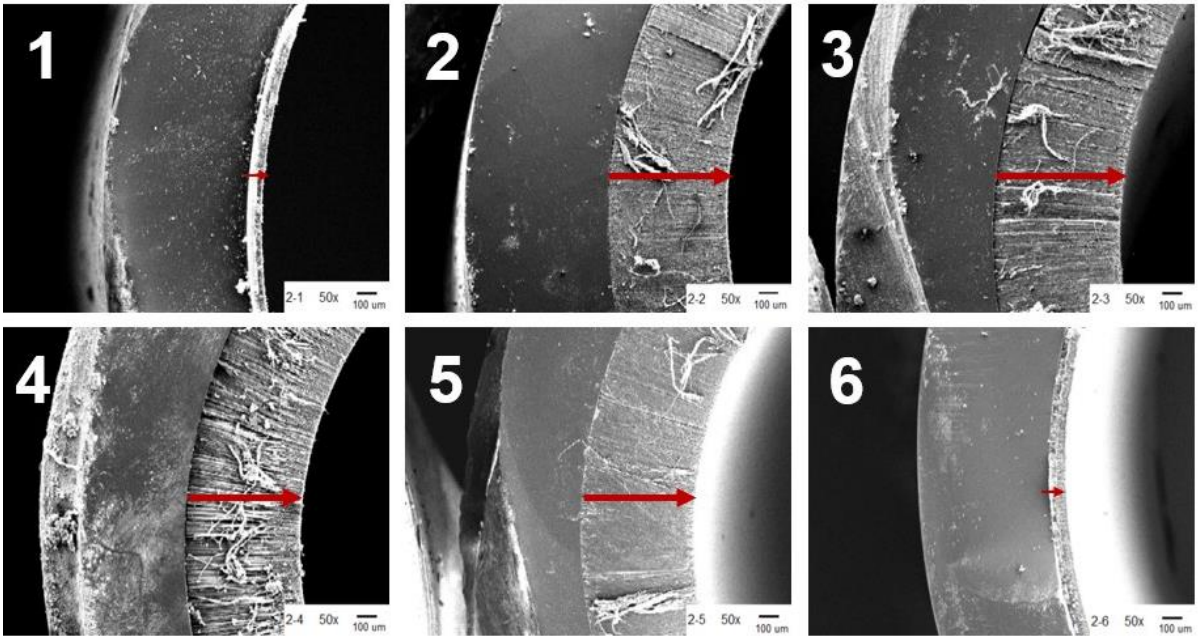

Figure 3. Cross-sectional SEM micrographs of MWCNT films synthesized at 800 °C with a carrier gas flow of 5000 sccm. The red arrows indicate the MWCNT thickness and growth direction.

As the flow rate is further increased to 7500 sccm (Figure 4), the MWCNT films reach their minimum observed lengths (table 1). The middle sections follow the established trend, exhibiting the shortest growth among the three tested flows.

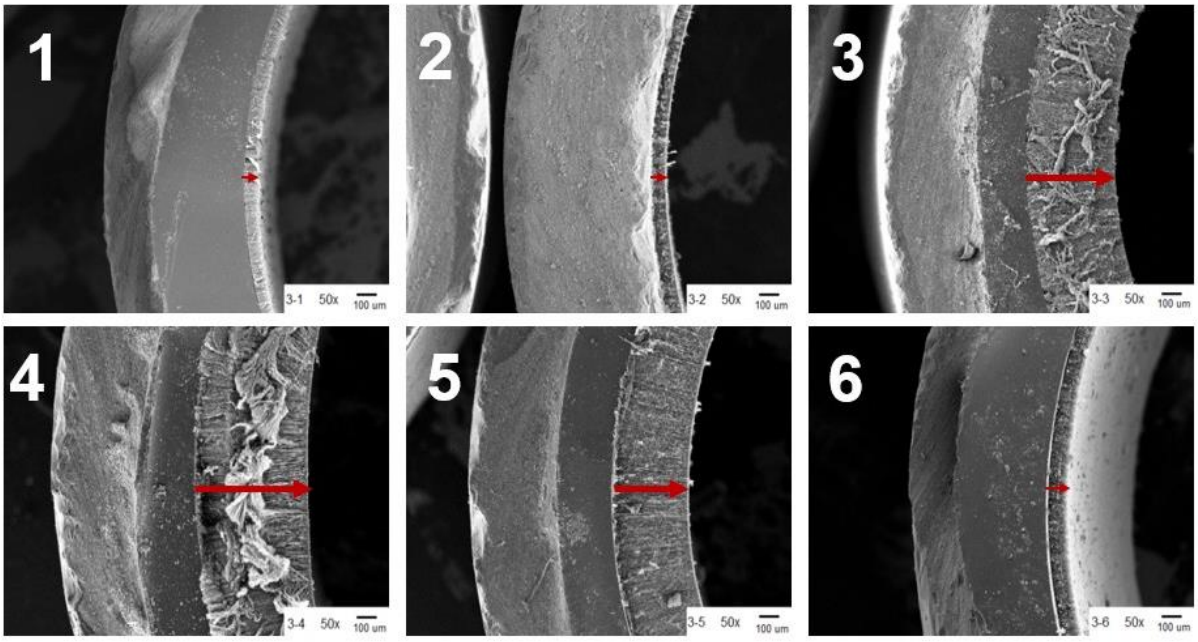

Figure 4. Cross-sectional SEM micrographs of MWCNT films synthesized at 800 °C with a carrier gas flow of 7500 sccm. The red arrows indicate the MWCNT thickness and growth direction.

3.3 Comparative Length Profiles

The spatial distribution of MWCNT lengths across the different flow regimes is summarized in the length profiles shown in Figure 5.

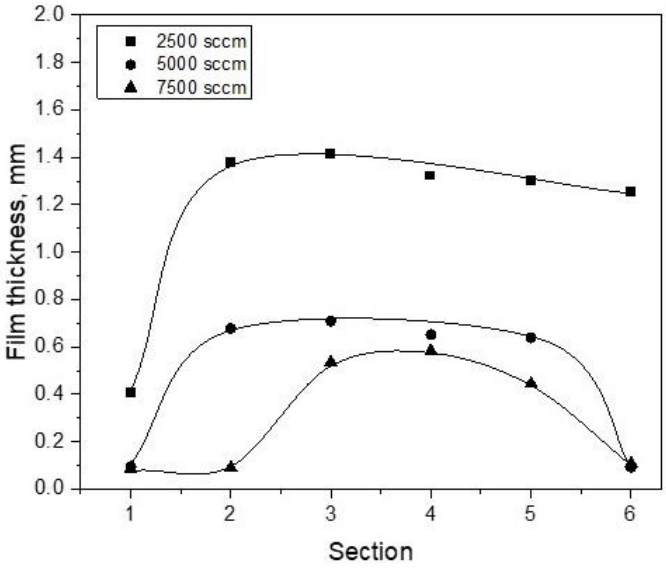

Figure 5. Comparative longitudinal length profiles of MWCNTs synthesized at flow rates of 2500, 5000, and 7500 sccm.

The data confirms that MWCNT growth is highly sensitive to the gas-phase dynamics. Lower flow rates promote the formation of longer nanotubes by optimizing the residence time and ensuring a high density of carbonaceous species over the catalytic particles. Conversely, high flow rates reduce the residence time of the precursor molecules within the hot zone of the furnace. This reduces the effective concentration of carbon fragments per unit area, effectively starving the catalyst sites and leading to shorter nanotubes.

3.3 Transmission Electron Microscopy Analysis

Figure 6 presents high-resolution transmission electron microscopy (HR-TEM) images of MWCNTs synthesized at varying reaction flows. All analyzed samples were extracted from section 3 of the reactor tubes to ensure spatial consistency. The micrographs reveal the formation of well-ordered MWCNTs, characterized by highly

aligned carbon layers with minimal visible structural defects. Structural quality was further evaluated using Fast Fourier Transform (FFT) analysis. For the MWCNTs grown at 2500 sccm (Figure 6c), the FFT patterns exhibit diffuse spots, suggesting a higher density of structural irregularities or lattice strain. Conversely, the samples synthesized at 5000 sccm and 7500 sccm (Figures 6f and 6i) display sharp, well-defined diffraction spots, confirming the presence of highly crystalline carbon nanostructures at these higher flow rates.

Structural quality was further evaluated using Fast Fourier Transform (FFT) analysis. For the MWCNTs grown at 2500 sccm (Figure 6c), the FFT patterns exhibit diffuse spots, suggesting a higher density of structural irregularities or lattice strain. Conversely, the samples synthesized at 5000 sccm and 7500 sccm (Figures 6f and 6i) display sharp, well-defined diffraction spots, confirming the presence of highly crystalline carbon nanostructures at these higher flow rates. The interlayer distance was quantified using intensity line scans derived from the FFT patterns (shown as insets in Figures 6c, 6f, and 6i). The d_{002} lattice spacing was estimated from these scans: at 2500 sccm, the d_{002} spacing was approximately 0.333 nm, slightly lower than the nominal value for ideal crystalline graphite (0.335 nm). At 5000 sccm and 7500 sccm, the estimated values were 0.344 nm and 0.347 nm, respectively. While the 2500 sccm sample shows a tighter spacing, the sharpness of the FFT spots and the overall lattice alignment suggest that the most structurally integrated and crystalline MWCNTs are produced at a flow rate of 5000 sccm. Collectively, these results suggest that while all flow rates produce aligned nanotubes, the 5000 sccm flow represents an optimal regime for synthesizing MWCNTs with the highest degree of structural crystallinity and lattice alignment.

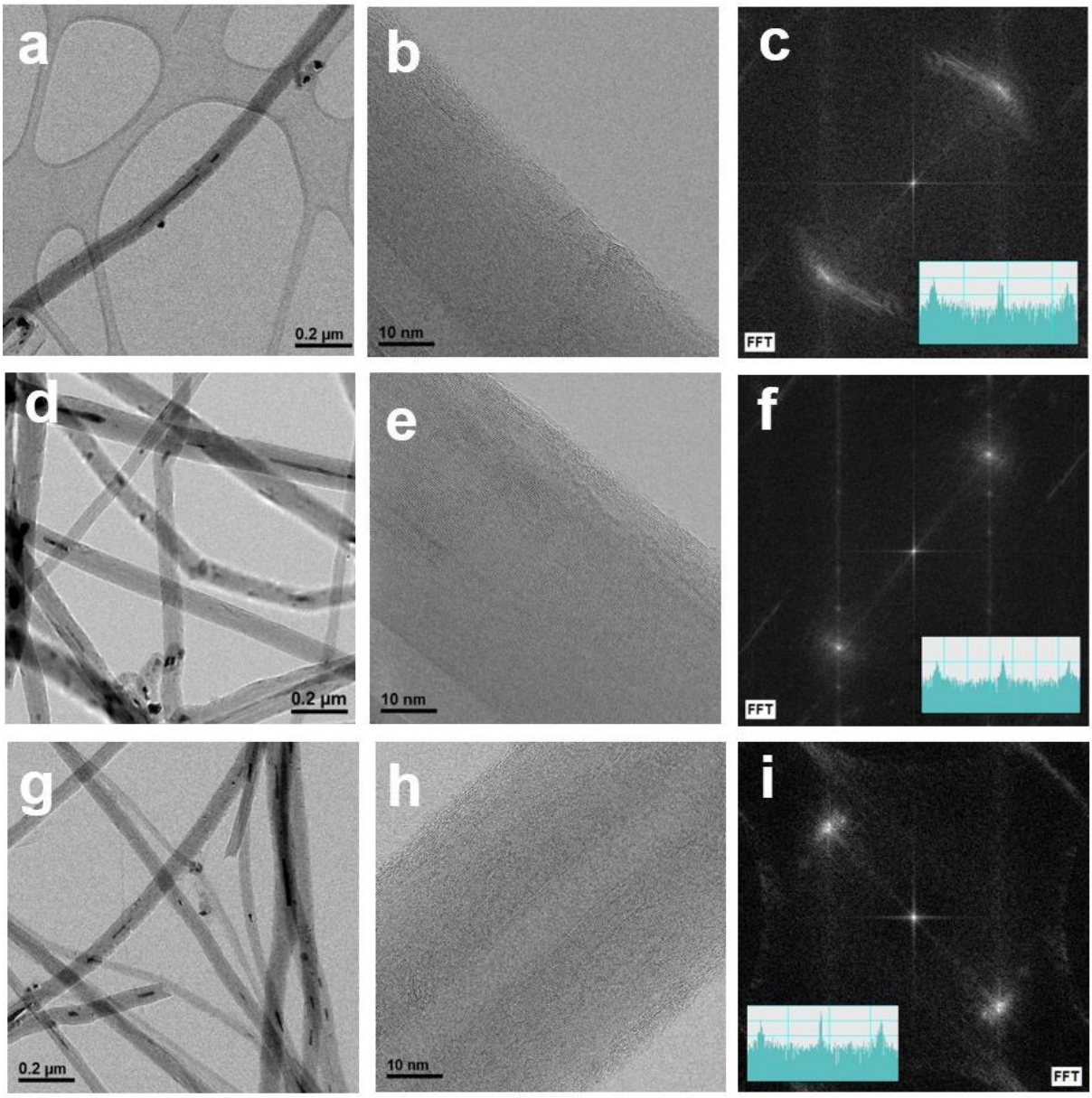

Figure 6. Representative HR-TEM micrographs and corresponding structural analyses of MWCNTs synthesized at varying reaction flows: (a–c) 2500 sccm, (d–f) 5000 sccm, and (g–i) 7500 sccm. The figure includes low-magnification overviews, high-resolution lattice imaging, and Fast Fourier Transform (FFT) patterns. Insets in (c), (f), and (i) display the FFT-derived intensity line scans used for d_{002} lattice spacing calculations.

3.4 Raman Spectroscopy Analysis

Figure 7 presents the Raman spectra of the MWCNTs synthesized at different flow rates. All spectra (Figures 7a–c) exhibit the characteristic peaks associated with MWCNTs: the D band (~1350 cm^{-1}), the G band (~1590 cm^{-1}) and the G' band (~2660 cm^{-1}) [22, 23]. The D band is associated with the A_{1g} symmetry breathing mode, typically attributed to structural defects and disordered carbon. The G band corresponds to the E_{2g} stretching mode of the sp^2-hybridized carbon atoms within the graphitic plane. The G' band corresponds to the first overtone of the D mode and is sensitive to the electronic structure and the stacking order of the carbon layers. The intensity ratio I_D/I_G serves as a primary indicator of structural disorder; a lower I_D/I_G value denotes a higher degree of graphitic order. Additionally, the $I_{G'}/I_G$ ratio provides insight into the smoothness of the carbon deposits, where higher values indicate fewer surface defects and higher structural integrity [24, 25].

Figures 7a–c specifically show the spectra for MWCNTs collected from the middle section of the reactor. The spatial distribution of the I_D/I_G and $I_{G'}/I_G$ ratios across all six sections for each flow rate is summarized in Figure 7d.

A clear trend in crystallinity and structural smoothness is observed along the length of the reaction tube. The central sections (3 and 4) consistently yielded the lowest I_D/I_G and highest $I_{G'}/I_G$ ratios, indicating that the most crystalline and ordered MWCNTs are formed in the center of the reactor. The end sections (1 and 6) exhibited the highest I_D/I_G and lowest $I_{G'}/I_G$ ratios, suggesting a higher concentration of amorphous carbon or structural defects at the tube's extremities. Comparing the three tested flow rates, the spectroscopic data confirms that the 5000 sccm flow

produces MWCNTs with the highest overall crystallinity, corroborating the HR-TEM findings in Section 3.3.

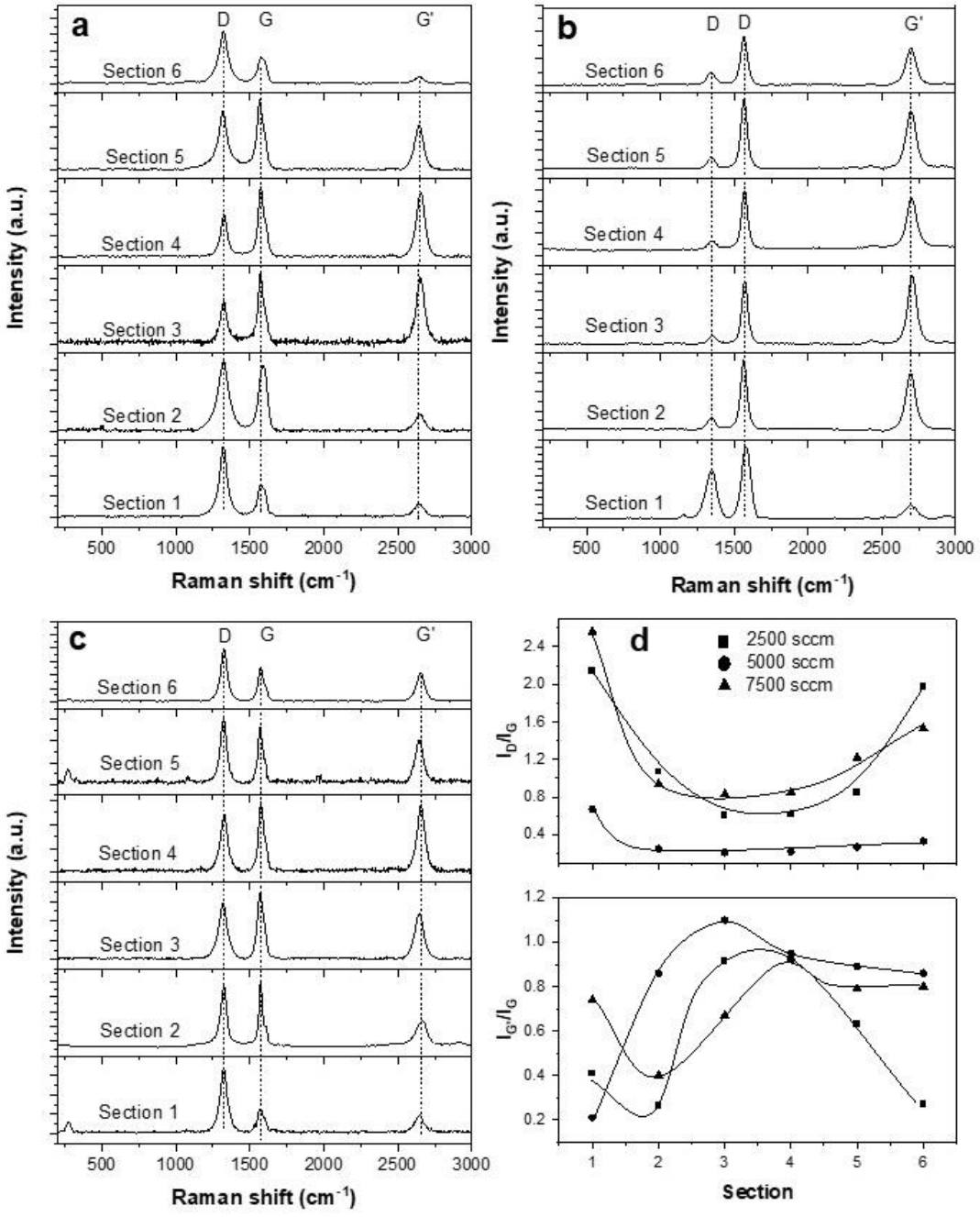

Figure 7. Raman spectra of MWCNTs synthesized at different carrier gas flow rates: **(a)** 2500 sccm, **(b)** 5000 sccm, and **(c)** 7500 sccm. **(d)** Corresponding I_D/I_G and $I_{G'}/I_G$ intensity ratios as a function of flow rate.

3.4 Thermogravimetric Analysis

The thermal stability and purity of the MWCNTs synthesized across different furnace sections and flow rates were evaluated via TGA. Figure 8 presents the weight-loss profiles and their corresponding derivatives, with numerical data summarized in Table 2. The residual mass, typically attributed to the encapsulated metal catalyst, was derived from the weight-loss curves in Figures 8a, 8c, and 8e. The highest catalyst concentrations were consistently observed in the outer regions (Sections 1 and 6). Conversely, the central regions (Sections 3 and 4) yielded MWCNTs with significantly lower metal content. Among the parameters tested, the 2500 sccm flow rate resulted in the lowest average metal residue, suggesting a more efficient carbon-to-catalyst ratio during growth at this velocity.

The derivative weight-loss curves (Figures 8b, 8d, and 8f) were used to identify the peak oxidation temperatures, a primary indicator of thermal stability. The MWCNTs produced at 5000 sccm exhibited the highest oxidation temperature (~649.6°C). This enhanced thermal stability suggests a higher degree of structural integrity and fewer graphitic defects [26]. These findings align with the HR-TEM observations and Raman spectroscopy results.

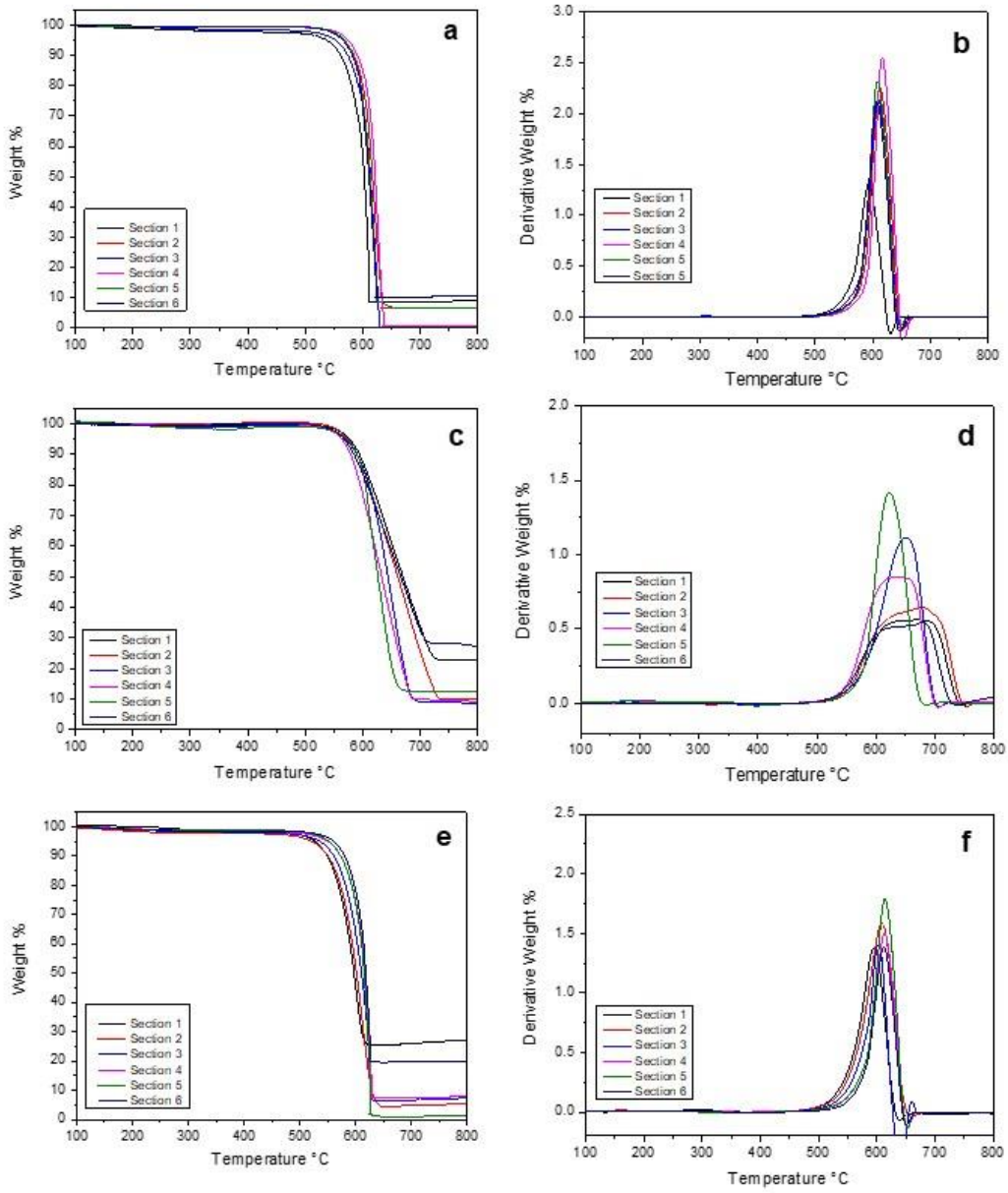

Figure 8. Thermogravimetric analysis (TGA) and derivative thermogravimetry (DTG) profiles of MWCNTs synthesized at various flow rates across different furnace sections: (a, b) 2500 sccm, (c, d) 5000 sccm, and (e, f) 7500 sccm. Left panels (a, c, e) display weight-loss percentage, while right panels (b, d, f) show the corresponding DTG curves.

Table 2. Residual mass (wt.%) of MWCNTs synthesized at various flow rates across furnace sections 1–6.

Flow rate (sccm)	1	2	3	4	5	6	Average
2500	10.10	7.20	0.10	0.90	7.00	9.20	5.75
500	22.10	10.30	8.10	9.10	12.20	21.40	14.87
7500	27.50	5.20	7.20	1.50	1.50	20.1	10.50

The spatial distribution of residual mass across the quartz tube followed a consistent 'U-shaped' trend, with the highest metal content located in Sections 1 and 6. This is likely due to the temperature gradients at the furnace boundaries, where lower temperatures may hinder efficient carbon-to-catalyst conversion compared to the isothermal center (Sections 3 and 4). Interestingly, while the 2500 sccm flow yielded the lowest overall metal residue, the 5000 sccm flow resulted in the highest thermal stability. This suggests that a moderate flow rate optimizes the structural integrity and crystallinity of the MWCNTs, even if a slightly higher amount of catalyst remains encapsulated within the graphitic walls.

3.5 X-ray Diffraction Analysis

The crystalline structure of the as-grown MWCNTs was characterized via XRD, with the resulting patterns shown in Figure 9a. The diffractograms exhibit a prominent peak at 2θ of ~26.0°, corresponding to the (002) reflection of the hexagonal graphite lattice. Additional lower-intensity signals observed at ~43.0°, 53.5 and 77.3° are indexed to the (100), (004), and (110) diffraction planes of graphite, respectively [27].

The Full Width at Half Maximum (FWHM) of the (002) reflection is a sensitive indicator of structural quality; it is influenced by the interlayer spacing (d_{002}) and lattice distortions arising from defective graphene stacking. Generally, a narrower FWHM signifies a more ordered graphitic structure with larger crystalline domains [28]. Figure 9b illustrates the FWHM values calculated for the (002) signal across the various flow rates. The 5000 sccm flow rate produced the narrowest FWHM, indicating superior crystallinity and more developed graphitic walls. This high degree of structural order at 5000 sccm aligns with the previously discussed TGA stability, Raman spectroscopy and HR-TEM observations, confirming this flow rate as the optimal condition for high-quality MWCNT growth.

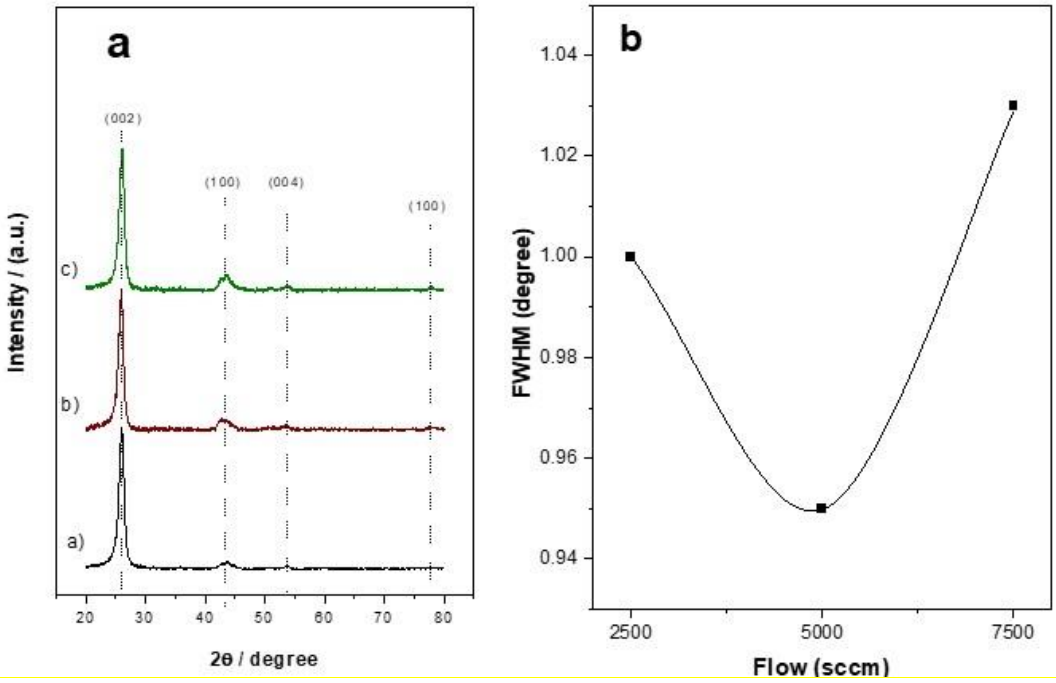

Figure 9. (a) XRD patterns of MWCNTs synthesized at flow rates of 2500, 5000, and 7500 sccm, showing characteristic graphitic reflections. **(b)** Full width at half

maximum (FWHM) values of the (002) diffraction peak as a function of the reaction flow rate, indicating variations in structural crystallinity.

The choice of α-pinene ($C_{10}H_{16}$) as a carbon source offers several advantages over traditional petroleum-derived hydrocarbons like ethylene or benzene. As a major component of turpentine and a primary botanical terpene, α-pinene is a renewable, biomass-derived precursor, making the synthesis process more environmentally sustainable. Chemically, the bicyclic structure of α-pinene facilitates a unique decomposition pathway. Upon entering the high-temperature zone (800 °C), the strained four-membered ring in the pinene molecule undergoes rapid thermal ring-opening and subsequent fragmentation. This process generates a high density of reactive intermediate species—such as isoprene-like fragments—which serve as the building blocks for the hexagonal carbon lattice of the MWCNTs. Furthermore, the high carbon-to-hydrogen ratio in α-pinene (10:16) provides a rich carbon environment, which, when balanced with the appropriate flow rate, promotes the rapid vertical alignment and high growth rates observed in this study. This demonstrates that bio-renewable terpenes are not only "green" alternatives but are also highly efficient precursors for high-quality carbon nanotube production.

4. Conclusions

High-crystalline, millimeter-long multi-walled carbon nanotubes (MWCNTs) were successfully synthesized via the spray pyrolysis of an α-pinene/ferrocene mixture. The investigation into carrier gas flow rates revealed a significant influence on both the growth kinetics and the structural integrity of the resulting nanotubes. The carrier gas flow rate is inversely proportional to nanotube length. The maximum length of 1.416 mm was achieved at the lowest flow rate of 2500 sccm. Increasing the flow to 5000 and 7500 sccm resulted in a reduction of length to 0.708 mm and 0.584 mm, respectively. While the 2500 sccm flow favored longitudinal growth, comprehensive characterization via Raman spectroscopy, XRD, and TGA confirmed that the 5000 sccm flow rate yielded the highest crystallinity and thermal stability. This suggests that a moderate flow rate optimizes the balance between precursor residence time and graphitic ordering. Analysis across the reactor zones indicated that structural features and dimensions remain remarkably consistent throughout the quartz tube, with the exception of the entrance (Section 1). In this initial zone, both length and crystallinity were substantially lower, likely due to the thermal gradients and the dynamics of initial catalyst activation.

Overall, this study demonstrates that α-pinene is a highly effective green precursor for the rapid production of MWCNTs, with the carrier gas flow serving as a critical reaction parameter to prioritize either nanotube length or crystalline perfection.

Funding

This work was supported by the Scientific Research Council - Universidad Michoacana de San Nicolás de Hidalgo.

Author Contributions

Alexis Pérez Gasquez y Marín: methodology; investigation; writing – original draft. Julián López-Tinoco: formal análisis; visualization; validation; writing – original draft. Javier Lara-Romero: conceptualization, visualization; methodology; formal analysis; writing – original draft; writing – reviewing & editing. Ricardo Rangel-Segura: validation; investigation; writing – original draft. Rafael Huirache-Acuña: methodology; validation. Dario J. Stacchiola: conceptualization; methology; formal analysis.

Data Availability Statement

Data generated and analyzed during this study is available from the corresponding author upon reasonable request.

References

1. Zhuang, Z.; Chang, J.; Fan, J.; Li, M., Dumitrică, T.; Xu, H. Mechanical properties of knitted carbon nanotube sheet: A molecular dynamics study. Diamond and Related Materials, **2025**, 152, 112005.
2. Voronin, K. V.; Ermolaev, G. A.; Burdanova, M. G.; Slavich, A. S.; Toksumakov, A. N.; Yakubovsky, D. I.; Volkov, V. (2024). Programmable carbon nanotube

networks: controlling optical properties through orientation and interaction. Advanced Science, **2024**, 11, 36, 2404694.

3. Sánchez-Romate, X. F.; Jiménez-Suárez, A.; Ureña, A. Electrical properties of carbon nanotubes. In Handbook of carbon nanotubes, **2022** (pp. 1-35). Cham: Springer International Publishing.
4. Krasley, A. T.; Li, E.; Galeana, J. M.; Bulumulla, C.; Beyene, A. G.; Demirer, G. S. Carbon nanomaterial fluorescent probes and their biological applications. Chemical Reviews, **2024**, 124, 6, 3085-3185.
5. Ijaz, H.; Mahmood, A.; Abdel-Daim, M. M.; Sarfraz, R. M.; Zaman, M.; Zafar, N.; Benguerba, Y. Review on carbon nanotubes (CNTs) and their chemical and physical characteristics, with particular emphasis on potential applications in biomedicine. Inorganic Chemistry Communications, **2023**, 155, 111020.
6. Conley, K.; Karttunen, A. J. Bridging the junction: Electrical conductivity of carbon nanotube networks. The Journal of Physical Chemistry C, **2022**, 126(40), 17266-17274.
7. Abdelhaleem, S.; Noun, M.; Yousif, N. M.; Shalaby, M. S. Impact of carbon nanotubes on superconducting properties and ferromagnetism of indium-doped Bi-2212 superconductors: Critical current density enhancement. Physica B: Condensed Matter, **2025**, 697, 416704.
8. Pinjari, S.; Bera, T., Kapur, G. S.; Kjeang, E. The mechanism and sorption kinetic analysis of hydrogen storage at room temperature using acid functionalized carbon nanotubes. International Journal of Hydrogen Energy, **2023**, 48, 5, 1930-1942.

9. Maheswaran, R.; Shanmugavel, B. P. A critical review of the role of carbon nanotubes in the progress of next-generation electronic applications. Journal of Electronic Materials, **2022**, 51, 6, 2786-2800.
10. Jiang, Q.; Wang, F.; Li, R.; Li, B.; Wei, N.; Gao, N.; Zhang, R. Synthesis of ultralong carbon nanotubes with ultrahigh yields. Nano Letters, **2023**, 23, 2, 523-532.
11. Christen H.M.; Puretzky A.A.; Cui H.; Belay K.; Fleming P.H.; Geohegan D.B.; Lowndes D.H. Rapid growth of long, vertically aligned carbon nanotubes through efficient catalyst optimization using metal film gradients. Nano Letters, **2004**, 4, 10, 1939-1942. https://doi.org/10.1021/nl048856f
12. Hata K.; Futaba D.N.; Mizuno K.; Namai T.; Yumura M.; Iijima S. Water-assisted highly efficient synthesis of impurity-free single-walled carbon nanotubes. Science, **2004**, 306, 5700, 1362-1364. https://doi.org/10.1126/science.1104962
13. Xiong G.Y.; Wang D.Z.; Ren Z.F. Aligned millimeter-long carbon nanotube arrays grown on single crystal magnesia. Carbon, **2006**, 44,5, 969-973. https://doi.org/10.1016/j.carbon.2005.10.015
14. McKee G.S.; Deck C.P.; Vecchio K.S. Dimensional control of multi-walled carbon nanotubes in floating-catalyst CVD synthesis. Carbon, **2009**, 47, 8, 2085-2094. https://doi.org/ 10.1016/j.carbon.2009.03.060
15. Cho W.; Schulz M.; Shanov V. Growth and characterization of vertically aligned centimeter long CNT arrays. Carbon, **2014**, 72, 264-273. https://doi.org/10.1016/j.carbon.2014.01.074

16. Asli, N. A.; Azhar, N. E. A.; Nurfazianawatie, M. Z.; Yusoff, K. M.; Omar, H.; Rosman, N. F.; Abdullah, S. Mechanism of vertically arrays of carbon nanotubes by camphor based catalysed in-situ growth. Fullerenes, Nanotubes and Carbon Nanostructures, **2022**, 30(4), 476-486.
17. Le, G. T.; Kyung, B.; Rouyre, E.; Ratchahat, S.; Chaiwat, W.; Charinpanitkul, T. Facile Preparation of Fe Mo Impregnated Catalyst for Carbon Nanotube Synthesis from Eucalyptus Oil. Journal of the Japan Institute of Energy, **2023**, 102, 9, 104-109.
18. Uthayakumar, H.; Radhakrishnan, P.; Shanmugam, K.; Kushwaha, O. S. Growth of MWCNTs from Azadirachta indica oil for optimization of chromium (VI) removal efficiency using machine learning approach. Environmental Science and Pollution Research, **2022**, 29, 23, 34841-34860.
19. Nimitha, K. C.; Abraham, J.; Reghunadhan, A.; George, S. C.; Thomas, S. Green Synthesis of Carbon Nanotubes. In Carbon Nanotubes for Energy and Environmental Applications, **2022**, (pp. 255-282). Apple Academic Press.
20. Lara-Romero J.; Ocampo-Macias T.; Martínez-Suarez R.; Rangel-Segura R.; López-Tinoco J.; Paraguay-Delgado F.; Chiñas-Castillo F. Parametric Study of the Synthesis of Carbon Nanotubes by Spray Pyrolysis of a Biorenewable Feedstock: α - Pinene. ACS Sustainable Chemistry & Engineering. **2017**, 5, 5, 3890–3896. https://doi.org/10.1021/acssuschemeng.6b03054
21. Lara-Romero J.; Calva-Yañez J.C.; López-Tinoco J.; Alonso-Nuñez G.; Jiménez-Sandoval S.; Paraguay-Delgado F.; Temperature Effect on the Synthesis of Multi-Walled Carbon Nanotubes by Spray Pyrolysis of Botanical Carbon Feedstocks: Turpentine, α-pinene and β-pinene. Fullerenes Nanotubes

and Carbon Nanostructures, **2011**, 19, 6, 483–496. https://doi.org/10.1080/1536383X.2010.494785

22. Lehman J.H.; Terrones M.; Meunier V.; Mansfield E.; Hurst K.E. Evaluating the characteristics of multiwall carbon. Carbon, **2011**, 49, 8, 2581–2602. https://doi.org/10.1016/j.carbon.2011.03.028
23. Dresselhaus M.S.; Dresselhaus G.; Saito R.; Jorio A. Raman spectroscopy of carbon nanotubes, Physics Report, **2005**, 409, 47–99. https://doi.org/10.1016/j.physrep.2004.10.006
24. Donato M.G.; Galvagno S.; Messina G.; Milone C.; Pistone A.; Santangelo S. Optimisation of gas mixture composition for the preparation of high quality MWCNT by catalytically assisted CVD. Diamond and Related Materials, **2007**, 16, 4-7, 095–1100. https://doi.org/10.1016/j.diamond.2006.12.018
25. Donato M.G.; Messina G.; Santangelo S.; Galvagno S.; Milone C.; Pistone A. Aid of Raman spectroscopy in diagnostics of MWCNT synthesised by Fe-catalysed CVD. Journal of Physics Conference Series, **2007**, 61, 1, 931–935. https://doi.org/10.1088/1742-6596/61/1/185
26. Martincic M.; Sandoval S.; Oró-Solé J.; Tobías-Rossell G. Thermal stability and purity of graphene and carbon nanotubes: key parameters for their thermogravimetric analysis (TGA). Nanomaterials, **2024**, 14, 21, 1754.
27. Maniwa Y.; Fujiwara R.; Kira H.; Tou H.; Nishibori E.; Takata M.; Y. Ando, Multiwalled carbon nanotubes grown in hydrogen atmosphere: An x-ray diffraction study. Physical Review B Condensed Matter and Materials Physics, **2001**, 64, 7, 073105. https://doi.org/10.1103/PhysRevB.64.073105
28. Andrews R.; Jacques D.; Qian D.; Dickey E.C. Purification and structural

annealing of multiwalled carbon nanotubes at graphitization temperatures. Carbon, **2001**, 39, 11, 1681–1687. https://doi.org/10.1016/S0008-6223(00)00301-8